PROCEEDINGS OF SCIENCE

ONLINE ICRC 2021
THE ASTROPARTICLE PHYSICS CONFERENCE
Berlin | Germany
37th International Cosmic Ray Conference
12–23 July 2021

Signatures of Recent Cosmic-Ray Acceleration in the High-Latitude γ-Ray Sky

Guðlaugur Jóhannesson[a,*] **and Troy A. Porter**[b] **on behalf of the Fermi Large Area Telescope Collaboration**

[a] *Science Institute, University of Iceland,*
Dunhaga 5, 107 Reykjavik, Iceland
[b] *W. W. Hansen Experimental Physics Laboratory and Kavli Institute for Particle Astrophysics and Cosmology,*
Stanford University, Stanford, CA 94305, USA
E-mail: gudlaugu@hi.is, tporter@stanford.edu

Cosmic-ray (CR) sources temporarily enhance the relativistic particle density in their vicinity over the background distribution accumulated by the past injection activity and propagation. If individual sources are close enough to the solar system, their localised enhancements may present as features in the measured spectra of the CRs and in the associated secondary electromagnetic emissions. The observation of large scale loop like structures in the radio sky is possible evidence of such nearby CR sources. If so, these loops should also be most visible in the high-latitude gamma-ray sky. Using $\sim$ 10 years of data from the Fermi Large Area Telescope, applying Bayesian analysis including Gaussian Processes, we search for extended enhanced emission associated with putative nearby CR sources in the energy range from 1 GeV to 1 TeV for the sky region $|b| > 30$ deg. We carefully control the systematic uncertainty due to imperfect knowledge of the interstellar gas distribution. Radio Loop IV is identified for the first time as a gamma-ray emitter and we also find significant emission from Loop I. Strong evidence is found for asymmetric features toward the Galactic centre that may be associated with parts of the so-called "Fermi Bubbles", and some evidence is also found for gamma-ray emission from other radio loops. Implications for the CRs producing the features and possible locations of the sources of the emissions are discussed.

37th International Cosmic Ray Conference (ICRC 2021)
July 12th – 23rd, 2021
Online – Berlin, Germany

*Presenter

PoS(ICRC2021)615

1. Introduction

The nature of cosmic-ray (CR) sources remains elusive despite over 100 years of observations. The body of evidence suggests that supernova remnants (SNRs) are the main source class [5] and in general, hypothesised sources of CRs have in common that they are usually discrete in both time and space. Following acceleration at the sources, the CRs propagate through the Galaxy, scattering off magnetic fields and thus removing all information about their origin from direct observations of CRs [11]. The γ-rays produced during their propagation, however, travel mostly unimpeded and provide location information that can be used to determine the distribution of CRs throughout the Galaxy [1, 3].

A study of the effect of spatio-/temporal discrete CR sources on predictions for γ-ray diffuse emission showed that for nearby discrete CR sources, excess emission over smooth CR source models is expected, which should be most evident for latitudes outside the Galactic plane [17]. Under the assumption that the source accelerates both nuclei and electrons, the excess is more prominent in the inverse Compton (IC) emission than the gas-related emission. For both processes, the enhanced emission is expected to be spectrally harder than the background, and would present as broadly distributed on the sky, likely with low surface brightness.

To extract this faint signal from 10 years of observations by the Large Area Telescope (LAT) of the high-latitude sky, we use Gaussian Processes (GPs) [10] to model the sky distribution of the structured gas and smooth IC components illuminated by the CRs. GPs utilise the high degree of dependence between neighbouring regions in the γ-ray sky that are expected to be spatially correlated because of the CR diffusion. Therefore, they are an appropriate tool for our analysis. This proceedings only lists a short summary of our model and results, the full details have already been published in [13]. A large fraction of the text in this proceedings is similar to that of the full article.

2. Data and Model

We use ~10 years of the most up-to-date data release of P8R3 photon events [7, 9], identical to that used in the second data release (DR2) [8] of the *Fermi*-LAT fourth source catalog (4FGL) [2]. The `ULTRACLEANVETO` photon event type and the associated `P8R3_ULTRACLEANVETO_V2` instrument response is used to reduce background emission as much as possible. The data are binned into a HEALPix[1] grid with N_{side} of 256 (order 8), having a spatial resolution of ~0.25°. We analyse the data independently in 4 coarse energy bins (1–3 GeV, 3–10 GeV, 10–60 GeV, and 60–1000 GeV) with each split further into 4 equally spaced logarithmic sub-bins. To avoid complications arising from modelling the Galactic plane, the analysis is restricted to latitudes $|b| > 30°$.

The model is based on the simple assumption that the γ-ray emission from the high-latitude sky can be separated into distinct components: (i) emission from point-like and slightly extended sources as listed in the 4FGL-DR2, (ii) structured component originating in interactions between CRs and the interstellar gas, and (iii) a smooth component comprising emissions by interactions between CRs and the ISRF, as well as from unresolved sources and irreducible background in the

[1] https://healpix.jpl.nasa.gov/

Table 1: Parameters used for the determination of the different gas templates based on dust based observations.

Dust map	α	X_d^{a}	d_0^{b}
τ_{353}^{c}	1.0	1.14×10^{26}	-2.6×10^{-7}
Tau[f]	1.2	1.64×10^{25}	1.6×10^{-7}
	1.4	4.17×10^{24}	4.6×10^{-7}
Radiance[d]	1.0	4.8×10^{27}	4.4×10^{-11}
Rad[f]	1.2	2.9×10^{26}	4.6×10^{-9}
	1.4	4.8×10^{25}	1.3×10^{-8}
A_v^{e}	1.0	8.6×10^{20}	−0.095
Av[f]	1.2	9.5×10^{20}	−0.011
	1.4	1.1×10^{19}	0.062

[a] In appropriate units so the output column density is cm^{-2}.

[b] In units of the dust map, see below.

[c] COM_CompMap_Dust-GNILC-Model-Opacity_2048_R2.01.fits, no units.

[d] COM_CompMap_Dust-GNILC-Radiance_2048_R2.00.fits, in units of $\mathrm{W\ m^{-2}\ sr^{-1}}$.

[e] COM_CompMap_Dust-DL07-AvMaps_2048_R2.00.fits, in units of magnitudes.

[f] Identifier for the different maps

data. For the first component, the source properties are kept fixed to that listed in the 4FGL-DR2. We model the gas column density distribution using four different tracers: the HI4PI 21-cm H I line emission [12], the dust optical depth at 353 GHz (τ_{353}), dust radiance [14], and optical extinction A_v [15]. For each of the four gas tracers, template maps are generated under different assumptions for converting the respective data to gas column densities. The H I data are converted to column densities under the assumption of a uniform spin temperature of $T_S = 100$ K and $T_S = 50$ K [see, e.g., 4, for more details], respectively. For the dust emission, D, the gas column density, G, is calculated using

$$G = X_d \, (D - d_0)^{1/\alpha} \tag{1}$$

where X_d is the dust-to-gas ratio, d_0 is a global offset, and α accounts for possible non-linearity in the conversion from gas to dust. For this analysis, the value of α is chosen to be one of 1.0, 1.2, and 1.4 and the values of X_d and d_0 are determined using a maximum likelihood fit of Eq. 1, assuming G is given by the optically thin H I data for $|b| > 30°$. The resulting parameters are given in Table 1.

To account and search for possible non-uniformity in the density of CRs, the directional emissivity of the gas component and the intensity of the smooth component are modelled using GPs. The spatial binning of the sky for the GPs are based on the HEALPix pixelisation, using an N_{side} parameter of 4 and 8 for the directional gas emissivity and intensity of the smooth component, respectively. The resolution, and hence the characteristic size of the GPs, is deliberately kept larger than the size of the LAT point-spread-function (PSF). To avoid sharp edges at the pixel boundaries, the emissivity and intensity values are interpolated to a HEALPix grid with the same resolution as the data ($N_{side} = 256$) using the HEALPix interpolation facility. The analysis is Bayesian in nature and parameter sampling and optimisation is performed using the Stan platform for statistical

modelling[2]. The analysis is performed independently in the northern and southern hemispheres (NH and SH, respectively) for each coarse energy bin. To allow for spectral freedom within each coarse bin, the spectrum for the emissivity and smooth component is modeled as a power-law, where a single index is applied for each component per analysis.

Using results from simulations (not shown here) we found that imperfections in the gas maps are the largest contributors to the uncertainty of the analysis, contributing up to and above 50% in the worst cases. The individual gas templates listed above are not expected to give a perfect representation of the structured emissions in the *Fermi*-LAT data. However, it has been shown that a linear combination of these maps can provide a good description of the gas-related γ-ray emission for small regions of the sky [e.g., 1, 3]. It is also known that the likelihood is a good indicator of the best-fit gas maps. Therefore, for the final LAT data analysis we will use a composite gas column density map created by segmenting the sky into a HEALPix grid with $N_{\rm side}$ of 8 and selecting in each pixel the gas template whose model is best according to the Akaike information criterion [6] for that region after analysing the LAT data independently with each gas map from Table 1. To avoid sharp boundaries, this coarse grid is interpolated to the original resolution of the templates, resulting in a linear combination of the maps for all directions, except those directly underneath the centre of the coarser pixels. This was shown to reduce the uncertainty caused by the gas map to $\sim$ 20%, which is still the dominant source of systematic uncertainty and larger than the statistical uncertainty which is $\sim$ 10%.

3. Results

Figure 1 shows the results of our analysis for the directional emissivity and smooth intensity. The results for the directional emissivity are statistically consistent with being constant, apart from an elongated feature visible between $\sim 340^\circ$ and $\sim 40^\circ$ longitude and $\sim 30^\circ$ and $\sim 45^\circ$ latitude. This feature is brighter than the background by $\sim$ 40% and therefore larger than the estimated systematical error. Its statistical significance is estimated at $\lesssim 3\sigma$, and as such can only be considered a hint of a deviation from uniformity rather than a detection.

For the smooth intensity component, the most obvious features consist of extended emission toward $l \sim 0^\circ$ that appear at intermediate latitudes in both hemispheres with a spectrum that is considerably harder than the background. The feature in the NH is clearly offset to negative longitudes, while the one in the SH is offset to positive longitudes. The shape of the feature in the NH appears to be fairly independent of energy, and is slightly dimmer than that in the SH. The latter shows evidence of an energy dependent shape. For the lower energy bins, the SH feature appears as two extended regions with the lower latitude one being brightest. For the higher energy bins, the brightest part is centred more toward $l \sim 0^\circ$ and higher latitudes.

To illustrate the lower surface brightness features, Figure 2 shows the smooth intensity component with a reduced intensity range. Overlaid on the maps are traces of radio loops and spurs taken from [18], selecting only those that are visible for the regions of sky considered by our analysis. It is clear that there is evidence for emission from features labeled I and IV, while others are not as apparent in the map. This is the first time that radio Loop IV has been detected in high-energy

[2]https://mc-stan.org/

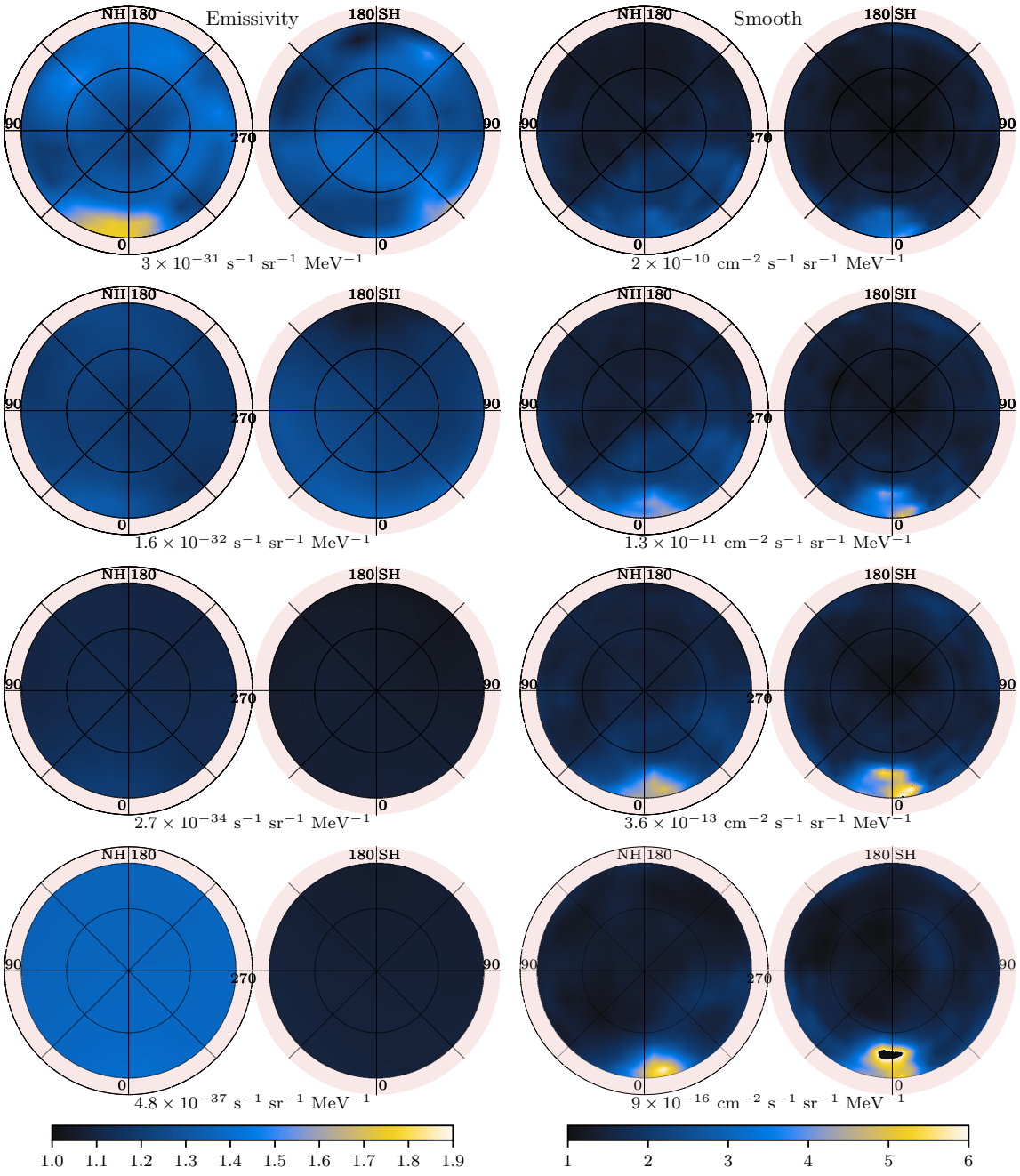

Figure 1: The directional gas emissivity (left column) and smooth component intensity (right column) resulting from analysis of LAT data using the final gas map. The maps are in orthographic projection with NH to the left and SH to the right. The directional emissivity and intensity are both evaluated at the geometric mean energy of each of the bins, from top to bottom: 1.7 GeV, 5.5 GeV, 24 GeV, and 240 GeV. The fractional colour scale is shown at the bottom of each column and the units of the maps are written below each panel.

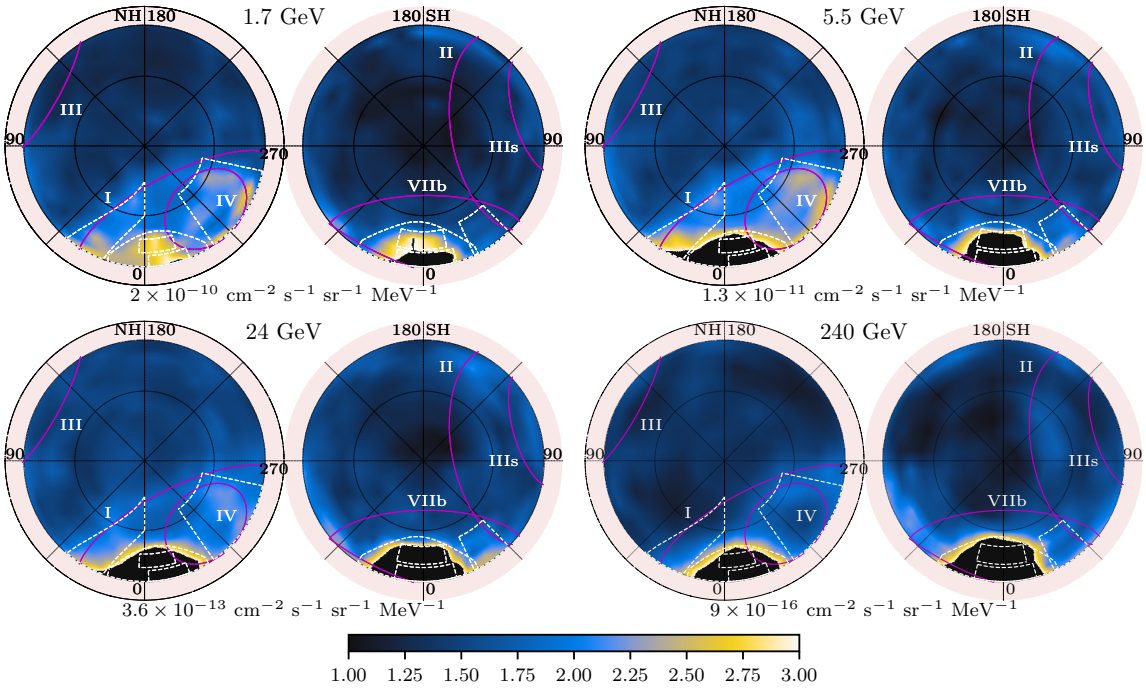

Figure 2: The smooth intensity component evaluated at the geometric centre of each of the energy bins used in the analysis. The range is reduced compared to Figure 1 and saturated pixels are shown as black. The magenta curves outline structures visible in radio synchrotron maps: the location and labels come from [18]. The dashed white lines enclose regions that we determine the individual spectra (see Figure 3 below). The maps are shown in orthographic projection, with the NH to the left and SH to right, centred on the poles. The fractional scale for the maps are identical, with the units given below each panel.

γ-rays. It is also clear that these features are softer than the overall background, because they are not visible at higher energies. The circular outline for radio Loop I seems to deviate from the γ-ray enhancement around $l \sim 315°$, where Loop IV becomes more prominent. Loop IV also seems to be centrally filled, at least for the lowest two energy bins. There also seems to be an enhancement towards $l \sim 35°$ in the SH with $-30° \lesssim b \lesssim 50°$ at the base of Loops II and VIIb. The spatial extent of this feature is smaller than that of Loops I and IV, but its magnitude is larger than expected from the systematic uncertainty estimated from the simulations making it likely a real feature.

To expand on the characteristics for the bright features in the smooth component described above, we determine the spectral content for the individual features using the white dashed outline regions shown in Figure 2. The resulting isotropic[3] subtracted spectral intensities are shown in Figure 3. For the features associated with the Loop I and IV overlays (top left panel), the spectra are essentially the same and very similar to that of the isotropic component, while the feature visible at the base of Loops II and VIIb is clearly harder. Meanwhile, the aggregate spectra for the NH/SH blobs toward $l \sim 0°$ are similar (top right panel), and generally harder than the loop-associated features, even the harder feature at the base of Loops II and VIIb. However, when we separate into approximately comparable 'lower/higher' latitude sub-regions (see Figure 2), in the bottom panel

[3]Estimated as the lowest intensity of the smooth component in each energy bin

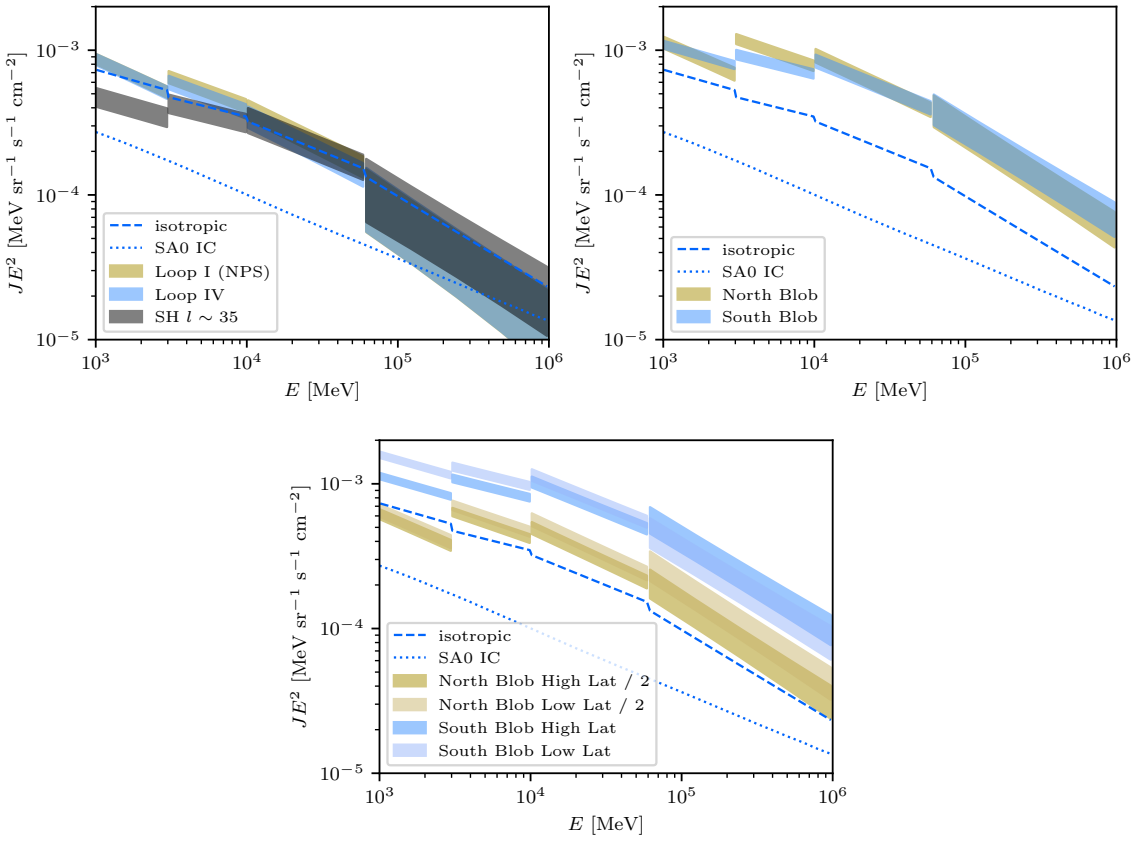

Figure 3: Spectral intensities derived for the bright smooth component regions delineated by the white lines in Figure 2. Panels: top left, loop-associated; top right, NH/SH blob total; bottom, NH/SH blobs split into low/high-latitude sub-regions. Note that the NH blob sub-regions are scaled down by a factor 0.5 for clarity. All panels also show the estimated isotropic spectrum and the IC prediction from the SA0 model[4].

we can see that the spectral characteristics for these blobs are different. Specifically, the NH blob lower/higher latitude spectra are very close in shape. On the other hand, the SH blob lower/higher latitude spectra are different. The low-latitude region has a similar spectrum to that for the NH blobs, whereas the high-latitude region is noticeably harder than all other regions.

4. Discussion

The brightest structures that we detected with the smooth intensity component are hard emission features located towards the GC that are offset to negative longitudes in the NH, and positive longitudes in the SH. These features are spatially consistent with the higher latitude emissions attributed to the FBs, and our results are qualitatively consistent with other work. The emissions that we obtain are spectrally harder than the surrounding background, with the average spectral features in the NH and SH similar. The feature in the SH shows evidence of spectral evolution, with

[4]A specific GALPROP model tuned to local observations of CRs [16]

the emission at $b \sim 35°$ being softer than the emission at $b \sim 45°$. No such evolution is evident for the feature in the NH.

We also detect significant emission from the radio Loops I and IV. The intensities of these individual loops in γ-rays are comparable, and they extend to $\gtrsim$100 GeV energies. Such detection contrasts with the situation in X-rays and radio, where Loop IV is much dimmer than Loop I. The hard spectrum of the γ-ray emission suggests a leptonic origin and, given their nondetection in the directional emissivity, indicates that these structures are located beyond most of the neutral gas at distances of $\gtrsim$ 200 pc. We also detect a marginally significant signal from the bases of Loops II and VIIb towards $l \sim 35°$. This enhancement is of similar magnitude as that of Loops I and IV, but its spectrum is significantly harder. There is also a faint signal detected toward this direction in the directional emissivity, but it is consistent with expected fluctuations from inaccuracies in the gas map. Nevertheless, this emission could come from a recent and fairly local CR injection event.

References

[1] Abdo, A. A., Ackermann, M., Ajello, M., et al. 2010, ApJ, 710, 133

[2] Abdollahi, S., Acero, F., Ackermann, M., et al. 2020, ApJS, 247, 33

[3] Ackermann, M., Ajello, M., Baldini, L., et al. 2011, ApJ, 726, 81

[4] Ackermann, M., Ajello, M., Atwood, W. B., et al. 2012, ApJ, 750, 3

[5] Ackermann, M., Ajello, M., Allafort, A., et al. 2013, Science, 339, 807

[6] Akaike, H. 1974, IEEE Transactions on Automatic Control, 19, 716

[7] Atwood, W. B., Baldini, L., Bregeon, J., et al. 2013, ApJ, 774, 76

[8] Ballet, J., Burnett, T. H., Digel, S. W., & Lott, B. 2020, arXiv e-prints, arXiv:2005.11208

[9] Bruel, P., Burnett, T. H., Digel, S. W., et al. 2018, arXiv e-prints, arXiv:1810.11394

[10] Cressie, N. 1993, Statistics for Spatial Data (Wiley)

[11] Grenier, I. A., Black, J. H., & Strong, A. W. 2015, ARA&A, 53, 199

[12] HI4PI Collaboration, Ben Bekhti, N., Flöer, L., et al. 2016, A&A, 594, A116

[13] Jóhannesson, G., & Porter, T. A. 2021, arXiv e-prints, arXiv:2104.13708

[14] Planck Collaboration, Aghanim, N., Ashdown, M., et al. 2016, A&A, 596, A109

[15] Planck Collaboration, Ade, P. A. R., Aghanim, N., et al. 2016, A&A, 586, A132

[16] Porter, T. A., Jóhannesson, G., & Moskalenko, I. V. 2017, ApJ, 846, 67

[17] —. 2019, ApJ, 887, 250

[18] Vidal, M., Dickinson, C., Davies, R. D., & Leahy, J. P. 2015, MNRAS, 452, 656